M. J. Roos [0]; S. M. Bleser [0]; L. Hernandez [0]; G. M. Diederich; M. E. Siemens [0]; M. Wu [0]; B. J. Kirby [0]; B. L. Zink 🕶 🕕



Journal of Applied Physics 133, 223901 (2023) https://doi.org/10.1063/5.0144371





CrossMark

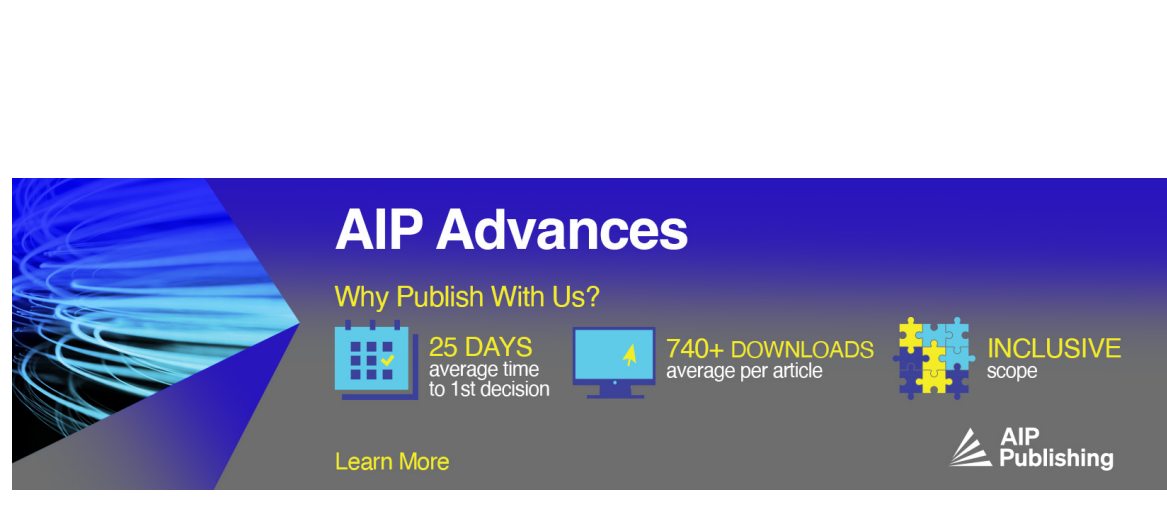
# Articles You May Be Interested In

The pairing relations for the magneto optical spectra of tetracene monovalent plus and minus ions J. Chem. Phys. (August 2008)

Negative spin Hall angle and large spin-charge conversion in thermally evaporated chromium thin films Journal of Applied Physics (March 2022)

Nonadditivity extension of the Kirkwood-Buff surface tension formula

J. Chem. Phys. (August 2008)



Cite as: J. Appl. Phys. 133, 223901 (2023); doi: 10.1063/5.0144371 Submitted: 29 January 2023 · Accepted: 17 May 2023 · Published Online: 8 June 2023







#### I. INTRODUCTION

Understanding in which regimes spin information can be transmitted through insulating magnetic materials is currently a major area of study in spintronics. The focus is often on materials with predominantly antiferromagnetic exchange interactions, whether these result in a ferrimagnetic state such as in yttrium iron garnet (Y<sub>3</sub>Fe<sub>5</sub>O<sub>12</sub> or YIG), or in a bulk antiferromagnetic state such as nickel oxide (NiO), chromium dioxide (Cr2O3), or iron oxides such as hematite (Fe<sub>2</sub>O<sub>3</sub>). This spin transport is measured

using a range of experimental techniques including spin pumping,<sup>2-4</sup> the spin Seebeck effect,<sup>5,6</sup> and non-local resistance measurements. 6-19 In these experiments, charge transport through the nominally insulating ferri- or antiferromagnetic films is assumed to be negligible, though some authors have demonstrated very clearly that in thin epitaxial YIG films, the bandgap is reduced from the bulk value  $E_g = 2.8 \,\text{eV}$  to near  $2.0 \,\text{eV}$ . This has important impact on non-local voltage measurements, particularly when large currents are used to excite nonlinear effects.

In many of these experiments, disorder in the magnetic state plays an important role, and in the most dramatic cases, researchers have explored spin transport in amorphous systems including amorphous films prepared with the same ratio of Y, Fe, and O atoms as ordered YIG (often abbreviated a-YIG, though here we use a-Y-Fe-O, since the term "garnet" is a specific reference to a crystalline state).21-25 Theoretical predictions of spin transport in disordered magnets have also been presented, though the conditions assumed for the disordered magnetic systems studied are not exactly mapped to the properties of a-Y-Fe-O.2 pumping<sup>21</sup> and spin Seebeck effect<sup>22</sup> measurements with a-Y-Fe-O inserted between an epitaxial YIG spin source and Pt spin detector showed spin diffusion length in the amorphous component between 1 and 10 nm, while our group previously explored nonlocal resistance measurements where large signals persisted over distances of many micrometers.<sup>23</sup> More recently, two groups have published non-local resistance results that put fairly stringent limits on the possibility of magnon-mediated spin transport in a-Y-Fe-O. 24,25 Gomez-Perez et al. compared non-local resistance using a combination of Pt and Cu strips, with separation of  $10 \mu m$ . These experiments showed the same sign of voltage when both Cu and Pt were used as the detector, as well as clear increase in voltage as a function of temperature, indicating that the signals have an origin in charge flow.<sup>24</sup> Yang et al. performed non-local and local (measuring transport in a vertical heterostructure), using Pt and permalloy electrodes. In both FMR-driven spin pumping and purely electrical experiments, these authors saw no evidence of long-distance spin transport, though they did report increased spin mixing conductance at the a-Y-Fe-O/permalloy interface.<sup>25</sup> In all these experiments, but particularly in the non-local resistance measurements, contributions from charge transport through the amorphous system must be carefully considered. As epitaxial YIG films are often prepared from annealing of amorphous precursors, and since a range of nanolithographic processing steps could introduce disorder at the interfaces with YIG and other materials, the charge transport and magnetic properties of disordered a-Y-Fe-O could potentially impact a broader range of the many spintronic devices based on YIG.

Amorphous semiconductors, including recently explored amorphous oxide semiconductors, <sup>30</sup> have been studied extensively and have a range of important applications for large-area electronic devices. The strong disorder in the system leads to Anderson localization of the electronic states near the band edges, and the boundary in energy between these localized states and extended states is the mobility edge. <sup>31,32</sup> In addition, a high level of defect states often forms near the middle of the gap, and nominally undoped amorphous semiconductors show electronic transport through these localized states via Mott's variable-range hopping mechanism, which has a characteristic temperature dependence (in the absence of correlated electron effects) at low temperature (*T*) given by

$$\sigma = \sigma_o \, e^{-(T_o/T)^{1/4}},\tag{1}$$

where  $\sigma_o$  and  $T_o$  are constants.

In this paper, we first present simple dc circuit models that clarify how dc leakage currents can generate non-local voltages in

these experiments and how they interact with various geometries of metal strips. We then present measurements of charge conductivity from 200 to 380 K, magnetic susceptibility, photoluminescence, and non-local resistance in a-Y-Fe-O. We compare the charge conductivity and non-local resistance measurements explicitly to amorphous germanium films. These results clearly show charge conductivity via the Mott variable-range hopping mechanism, indicating that both materials are best described as amorphous semiconductors. The non-local resistance measurements show clear correlations with the charge conductance in both a-Ge and a-Y-Fe-O. We also clarify the conditions for observation of spin transport in non-local resistance measurements in the presence of charge transport and compare non-local resistance measurements made using two common measurement techniques: quasi-dc current reversal and lock-in detection with a known range of ac frequencies. In spin transport experiments where the magnetic order can be manipulated to clearly isolate spin effects and when other potential complications can be controlled, these approaches have been previously shown to agree. 33 Data presented here shows that reactive components of the non-local measurement circuit can cause artifacts in the quasi-dc measurement that mimic the spin transport signal in certain geometries, causing serious challenges for studies of systems such as antiferromagnets and disordered spin systems where the magnetic order is not easily manipulated.

### II. EQUIVALENT CIRCUIT MODEL OF CHARGE LEAKAGE

Figure 1 shows a schematic view of a non-local spin transport experiment where spin is injected and detected via the spin Hall effect (SHE). Two strips of a metal film that supports spin-charge conversion (here characterized as a spin Hall effect, though any mechanism converting charge current to spin current could be mechanism converting charge current to spin current could be employed) are in contact with a spin transport medium as shown in Fig. 1(a). In the case of a purely insulating magnetic medium in Fig. 1(a). In the case of a purely insulating magnetic medium, in Fig. 1(a). In the case of a purely insulating magnetic medium, the spin can excite magnons that flow to the distant contact, length L away, and be detected via the inverse spin Hall effect when the spin current flows into the metal strip. If the spin medium also allows charge to flow, this leakage current can flow across the spin fransport medium to the (typically) much lower resistivity metal detector, eventually returning to the opposite charge terminal as shown in Fig. 1(b). Here we show two of the many possible of shown in Fig. 1(b). Here, we show two of the many possible current paths as black lines. Note that since electrons have negative in charge, the electron drift velocity direction is opposite to the charge, the electron drift velocity direction is opposite to the arrows shown, which indicate the direction of current flow. The portion of the current flowing along path  $i_{c,1}$  will generate spin  $\frac{-}{2}$ current according to the SHE. The portion of the current that follows path  $i_{c,2}$  and similar paths can lead to significant current density,  $\vec{J}$ , present in the detector strip. According to Ohm's law,  $\vec{E} = \rho \vec{J}$ , where  $\rho$  is the charge resistivity, this current density must be accompanied by an electric field  $\vec{E}$ , which is parallel to the current as indicated by the orange vector. This electric field leads to a voltage drop on the Pt wire, which is measured at the terminals,  $V_{\rm nl}$ . This voltage has the typical sign expected when current flows in a resistor (with positive  $V_{\rm nl}$  when positive  $I_{\rm bias}$  is applied, giving a positive slope on a plot of  $V_{\rm nl}$  vs  $I_{\rm bias}$ ). However, as shown in Fig. 1(c), when the current flowing in the sense of path  $i_{c,1}$  leads to a spin current that is injected downward into the transport

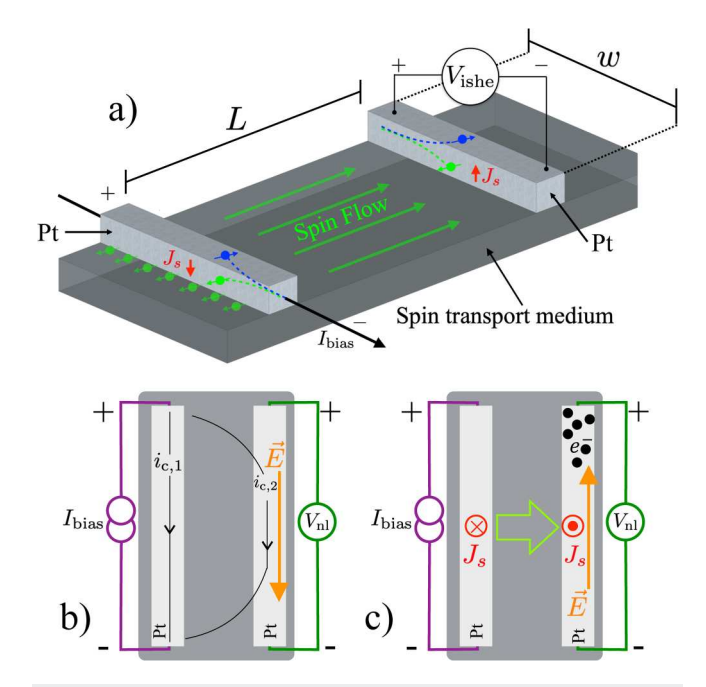


FIG. 1. (a) Schematic of SHE-driven non-local spin transport. Typically, two Pt strips with length w along the charge flow direction, separated by a distance L, are placed in contact with a spin transport medium. A charge current, Ibias, driven into the injector strip (here shown at left) is converted to spin current via the SHE. This is injected into the spin transport medium, where it travels to the distant Pt strip. The resulting spin current absorbed into this Pt detector generates a charge voltage via the ISHE. (b) A top-view schematic of a charge leakage contribution to a non-local voltage measurement. If the spin transport medium also allows charge flow, charge current can flow from the injector through the spin medium into the distant Pt strip. This travels down the typically much lower resistance Pt strip, generating a voltage with a positive sign with lead polarity chosen as shown by the + and - symbols. The charge then returns to ground by passing back through the spin medium. (c) Schematic view of spin transport in the same geometry, clarifying the direction of spin flow. The opposite sense of the spin flow in the injector and detector leads to a non-local voltage with the opposite sign from charge leakage.

medium, it flows through the medium and then upward into the detector. The inverse spin Hall effect (ISHE), assuming the detector has the same sign of the spin Hall angle as the detector, causes both spin up and spin down electrons to collect at the positive voltage measurement terminal when positive  $I_{\text{bias}}$  is applied, as indicated. In open circuit conditions for the voltage measurement on the detector strip, the electrons cause a charge accumulation that leads to an electric field. As indicated in the figure again with an orange vector, this electric field points in the opposite direction as the field in Fig. 1(b) and leads to the opposite sense of the potential difference. A measurement of this voltage as a function of bias current when the experiment is dominated by spin flow in the medium will show a slope of the IV curve that is negative. This is often taken as proof of spin transport, though we will show that certain purely electrical artifacts can also mimic this sign reversal.

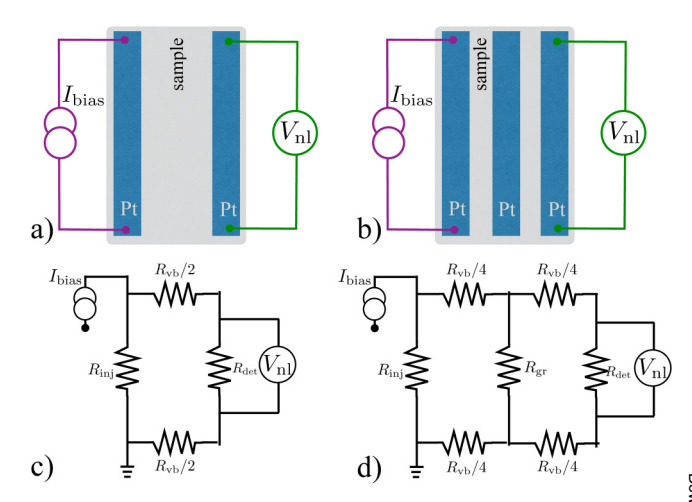


FIG. 2. Schematic views and circuit models describing dc charge leakage in SHE-driven non-local spin transport experiments. (a) A top-down schematic view of a typical lead arrangement where Pt strips are in contact with a sample spin transport medium. (b) A similar view with a third metallic strip added between the spin injector and the detector. (c) Simplified circuit model describing charge leakage in the standard two-strip geometry. When R<sub>vb</sub> is large compared to  $R_{\text{inj}}$  and  $R_{\text{det}}$ , a small portion of the total injected bias current flows on the right current path and generates a non-local voltage  $V_{\rm nl}$  via leakage. (d) A modified circuit model demonstrates the possible reduction in  $V_{nl}$  in dc from the third metal strip.

The simple view of charge flow in a SHE-driven non-local pransport experiment, shown in Fig. 2(a), can be represented with the lumped-element circuit model shown in Fig. 2(c). The requirement for the current to return to ground after any shunting by a nearby metallic strip means that, at an absolute maximum, the top half of the film is available to allow charge flow from the injector with resistance  $R_{\rm inj}$  to the detector with resistance  $R_{\rm det}$ , with the lower half returning the current to low potential. Thus, the parallel charge conductance path is formed with effective shunt resistors  $R_{\rm vb}/2$ , where  $R_{\rm vb}$  is the total resistance of the spin transport medium between the relevant contacts, determined in our case by measuring current flow in response to a voltage bias. This avoids thermal, thermoelectric, and other non-ideal effects in typically thermal, thermoelectric, and other non-ideal effects in typically very high resistance measurements. Any charge that flows across on the spin transport film travels through the metallic detector, producing the voltage drop measured as a non-local voltage,  $V_{\rm nl}$ , before returning to ground. We calculate this voltage using before returning to ground. We calculate this voltage using

$$V_{\rm nl} = I_{\rm bias} R_{\rm det} f \left( 1 - \frac{R_{\rm vb} + R_{\rm det}}{R_{\rm vb} + R_{\rm inj} + R_{\rm det}} \right),$$
 (2)

which represents the relevant current division with the addition of the factor f, which accounts for the difference between the actual charge flow paths and those used in this highly simplified lumped-element model. We expect f to be a small number, and the experiments below suggest it is on the order of 0.01 for our work.

When  $R_{\text{inj}}$ ,  $R_{\text{det}} < R_{\text{vb}}$  Eq. (2) is simply

$$V_{\rm nl} \simeq I_{\rm bias} \left( f \frac{R_{\rm inj} R_{\rm det}}{R_{\rm vb}} \right),$$
 (3)

and the term in parentheses is the expected non-local charge leakage resistance.

We observe that intermediate metal strips can potentially reduce the leakage current in dc, though also add capacitance and inductance to the circuit and make any ac or effectively ac measurements less clear to interpret. In dc, we can model such an insertion of a "guard rail" as shown in Fig. 2(b) using the circuit shown in Fig. 2(d). Here, the third metal strip, with resistance  $R_{gr}$ , provides an additional low resistance region in the middle of the sample. The film resistance between the injector and detector at each step is approximately halved, so we take  $R_{\rm vb}/4$  to be the film resistance in each branch of the circuit. Again applying simple current division, we can write the guarded leakage voltage as

$$V_{\rm nl,gr} = I_{\rm bias} R_{\rm det} f f^* \left( \frac{R_{\rm inj}}{R_{\rm inj} + R_{\rm eff}} \right) \left( \frac{R_{\rm gr}}{R_{\rm gr} + R_{\rm vb}/2 + R_{\rm det}} \right), \quad (4)$$

where the effective resistance of all elements other than  $R_{inj}$  is

$$R_{\rm eff} = \frac{R_{\rm vb}}{2} + \frac{R_{\rm gr}(R_{\rm vb}/2 + R_{\rm det})}{R_{\rm gr} + R_{\rm vb}/2 + R_{\rm det}},$$
 (5)

and  $f^*$  takes into account the different effective geometry of charge flow from the guard rail to the detector strip from the idealized model. As before, when  $R_{vb}$  is the largest resistance, Eq. (4) is

$$V_{\rm nl,gr} \simeq I_{\rm bias} \left( f \frac{R_{\rm inj} R_{\rm det}}{R_{\rm vb}} \right) \left( f^* \frac{4R_{\rm gr}}{R_{\rm vb}} \right),$$
 (6)

and the leakage resistance is reduced from the simple model of Eq. (3) by the factor  $4f^*R_{gr}/R_{vb}$ . Assuming that the charge conductivity of the sample medium is uniform, that  $f^* \simeq f$ , and with a value of  $R_{\rm gr}/R_{\rm vb}$  on the order of  $10^{-2}$  or smaller, this factor could cause a reduction of leakage voltage by several orders of magnitude for purely dc measurements. This overly simple model makes a number of somewhat speculative assumptions. Two-dimensional finite element calculations, on both simple lead configurations and the more complicated geometries used in experiments, show similarly dramatic reductions in dc charge leakage, though these also rest on the assumption of a uniform conducting medium.

#### III. EXPERIMENT

We prepared amorphous Y-Fe-O films by ambient temperature RF sputtering from a Y<sub>3</sub>Fe<sub>5</sub>O<sub>12</sub> target onto amorphous Si-N coated silicon substrates. We prepared amorphous germanium films via thermal evaporation of Ge from 99.999% pure source material in high vacuum (approximately 10<sup>-6</sup> Torr or  $1.3 \times 10^{-4}$  Pa) also onto amorphous Si-N coated Si substrates at a rate of approximately 0.13 nm/s. Note that at this deposition rate and base pressure, the films likely have significant defect atoms

included in the disordered matrix. For both a-Y-Fe-O and a-Ge we explored two methods for patterning metal leads to measure charge transport and test non-local spin transport. These were deposition of the sample film on Si-N/Si substrates with pre-patterned strips of 40 nm thick Pt with a 10 nm thick Cr sticking layer, and patterning of Pt and Cu strips on the top surface of the samples via e-beam lithography (EBL) and lift-off. For the EBL lead patterns, we also prepared the lead patterns on a highly insulating Si-N coated Si substrate with no other film added. Figure 3(a) is a scanning-electron micrograph top-view of an example of the EBL-patterned leads. Figure 3(b) shows a cross-sectional view of these lead patterns, which we produced with three different injector-detector separations and, for one separation, with an additional Cu lead. To form these, we used a PMMA layer (Microchem 950 PMMA A3) with Co-PMMA underlayer [MMA(8.5) MAA EL 6], each spun for 5s at 500 rpm then for 45s at 2000 rpm and baked at  $180\,^{\circ}$ C. We sputtered platinum leads after reaching base pressure  $4\times10^{-8}$  Torr at  $100\,\mathrm{W}$  in 3 mTorr of Ar, giving a growth rate of  $0.125\,\mathrm{nm/s}$ . We evaporated the Cu leads after reaching base pressure  $7\times10^{-7}$  Torr at a rate  $\cong 0.14\,\mathrm{nm/s}$ . Before the Cu deposition, the sample film surface was Ar plasma cleaned in a separate vacuum chamber for 1 min. vacuum chamber for 1 min.

The pre-patterned Pt strips are shown in an optical micrograph in Fig. 3(c) and in a schematic cross section in Fig. 3(d). These strips are a section of the Pt leads on thermal isolation platforms our group developed and uses for thermal characterization of thin films,<sup>34</sup> as was the case for our initial spin transport studies of a-YIG.  $^{23}$  The strips are  $40\,\mu\mathrm{m}$  wide, with a 10- $\mu\mathrm{m}$  separation between adjacent conductors, and a total length of  $\simeq$ 12 mm. Both the Cr and Pt were e-beam evaporated at similar base pressure and patterned via optical photolithographic lift-off.

and patterned via optical photolithographic lift-off.

For all transport measurements, the substrates are mounted on the cold finger of a sample-in-vacuum cryostat using gold-coated OFHC copper sample mounts. Leads are ultrasonically wirebonded and a radiation shield installed to ensure an isothermal sample environment. Transport measurements use standard computer-controlled source-meter equipment. Voltage-biased a-Ge and a-Y-Fe-O film resistance were measured with a Keithley 2400 sourcemeter. We compare two methods for measuring the non-local IV and R: the "quasi-dc" measurements using either the differential conductance or "delta mode" measurement features of the Keithley 2182a/6221 nanoyoltmeter and precision current source, Keithley 2182a/6221 nanovoltmeter and precision current source, and frequency-dependent ac measurements using a Stanford Research Systems 830 lock-in amplifier, using an external function generator and bias resistor to apply the ac bias current. Most experiments were performed at relatively low bias current and used a 90 k $\Omega$  bias resistor that is much larger than the  $\sim$ 1 k $\Omega$  resistance of the injector strips. To apply the largest bias currents (up to 7 mA), we used much smaller bias resistance (in some cases we used only the in-line lead resistance). Where this was done, we observed no qualitative change in the balance between in-phase and out-of phase components of the ac signal.

We performed photoluminescence measurements of a-Y-Fe-O by focusing the light from a 405 nm diode laser through a 0.40 NA objective onto the samples at a 30° angle from their surfaces to minimize back reflected excitation light in the measurement. The focused spot was roughly  $5\mu m$  in diameter and all measurements

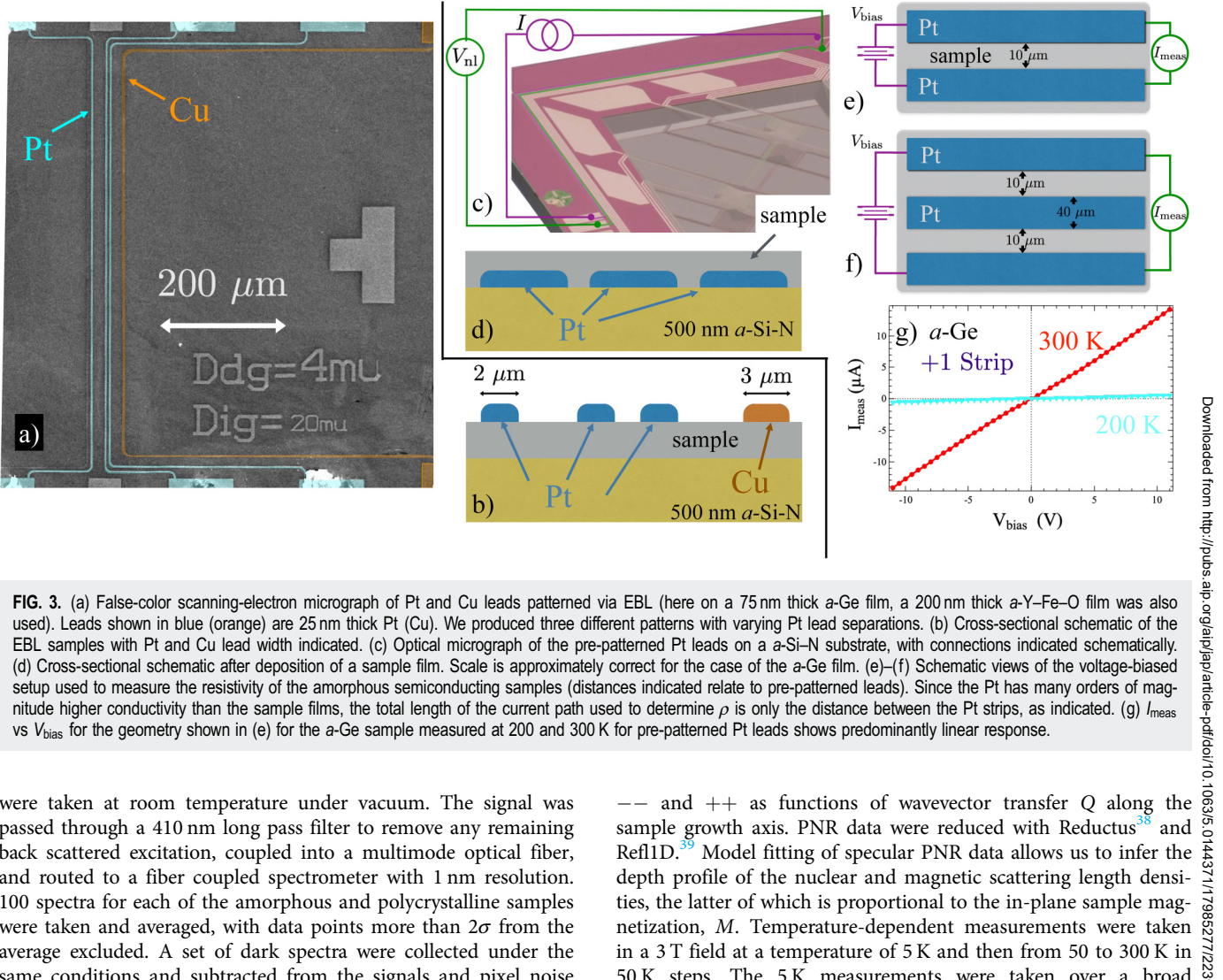


FIG. 3. (a) False-color scanning-electron micrograph of Pt and Cu leads patterned via EBL (here on a 75 nm thick a-Ge film, a 200 nm thick a-Y-Fe-O film was also used). Leads shown in blue (orange) are 25 nm thick Pt (Cu). We produced three different patterns with varying Pt lead separations. (b) Cross-sectional schematic of the EBL samples with Pt and Cu lead width indicated. (c) Optical micrograph of the pre-patterned Pt leads on a a-Si-N substrate, with connections indicated schematically. (d) Cross-sectional schematic after deposition of a sample film. Scale is approximately correct for the case of the a-Ge film. (e)-(f) Schematic views of the voltage-biased setup used to measure the resistivity of the amorphous semiconducting samples (distances indicated relate to pre-patterned leads). Since the Pt has many orders of magnitude higher conductivity than the sample films, the total length of the current path used to determine  $\rho$  is only the distance between the Pt strips, as indicated. (g)  $I_{meas}$ vs V<sub>bias</sub> for the geometry shown in (e) for the a-Ge sample measured at 200 and 300 K for pre-patterned Pt leads shows predominantly linear response.

were taken at room temperature under vacuum. The signal was passed through a 410 nm long pass filter to remove any remaining back scattered excitation, coupled into a multimode optical fiber, and routed to a fiber coupled spectrometer with 1 nm resolution. 100 spectra for each of the amorphous and polycrystalline samples were taken and averaged, with data points more than  $2\sigma$  from the average excluded. A set of dark spectra were collected under the same conditions and subtracted from the signals and pixel noise was smoothed with a moving average filter over 40 pixels.

We characterized the magnetic properties of the a-Y-Fe-O films using a commercial SQUID magnetometer, with automated temperature control from 2 to 400 K using a reciprocating sample method to increase the signal-to-noise ratio.<sup>37</sup> We measured a matching Si-N coated Si substrate to determine the magnetic background, which was subtracted from the total signal measured from the a-Y-Fe-O/Si-N/Si samples. We mounted samples in a laminar flow hood using dedicated non-metallic tools and clean gloves to minimize contamination from dust and other potential sources of spurious magnetic contributions.

We conducted polarized neutron relfectometry (PNR) measurements using the polarized beam reflectometer at the NIST Center for Neutron Research. An incident 0.475 nm neutron beam was polarized with magnetic moment parallel (+) or antiparallel (-) to a magnetic field, H, applied along the plane of the sample. We measured the spin analyzed non-spin-flip specular reflectivities in a 3 T field at a temperature of 5 K and then from 50 to 300 K in 50 K steps. The 5 K measurements were taken over a broad Q-range, while those at higher temperatures were taken only over a 1 C to range sufficient to characterize the lowest Q spin asymmetry (difference in ++ and -- divided by the sum) peak. The nuclear profile determined from the 5 K data was used for modeling of the higher temperature data.

## **IV. RESULTS AND DISCUSSION**

We begin by presenting magnetic characterization of the a-Y-Fe-O films. This material is perhaps most accurately described magnetically as a speromagnet, 40-42 where strong antiferromagnetic exchange interactions with randomized local anisotropy results in a magnetic state qualitatively similar to a spin glass. The central and most repeatable feature of this material, clearly seen in Fig. 4(a) and also observed in previous studies, 43,44 is the splitting between the magnetic susceptibility,  $\chi$ , vs T measured when the material is cooled to low T in zero field (ZFC) and that measured when

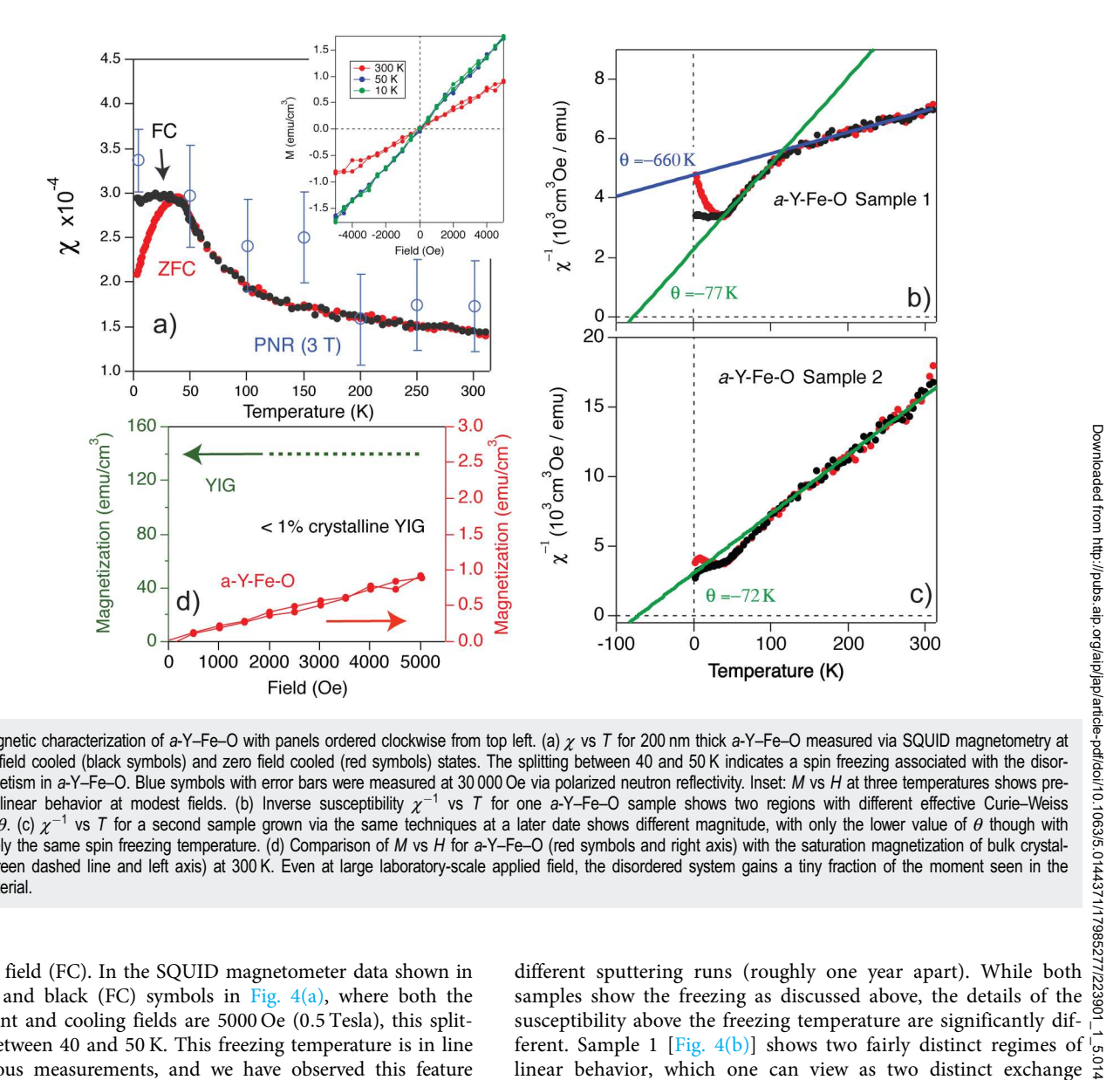


FIG. 4. Magnetic characterization of a-Y-Fe-O with panels ordered clockwise from top left. (a)  $\chi$  vs T for 200 nm thick a-Y-Fe-O measured via SQUID magnetometry at 5000 Oe in field cooled (black symbols) and zero field cooled (red symbols) states. The splitting between 40 and 50 K indicates a spin freezing associated with the disordered magnetism in a-Y-Fe-O. Blue symbols with error bars were measured at 30 000 Oe via polarized neutron reflectivity. Inset: M vs H at three temperatures shows predominantly linear behavior at modest fields. (b) Inverse susceptibility  $\chi^{-1}$  vs T for one a-Y-Fe-O sample shows two regions with different effective Curie-Weiss parameter,  $\theta$ . (c)  $\chi^{-1}$  vs T for a second sample grown via the same techniques at a later date shows different magnitude, with only the lower value of  $\theta$  though with approximately the same spin freezing temperature. (d) Comparison of M vs H for a-Y-Fe-O (red symbols and right axis) with the saturation magnetization of bulk crystalline YIG (green dashed line and left axis) at 300 K. Even at large laboratory-scale applied field, the disordered system gains a tiny fraction of the moment seen in the ordered material

cooled in a field (FC). In the SQUID magnetometer data shown in red (ZFC) and black (FC) symbols in Fig. 4(a), where both the measurement and cooling fields are 5000 Oe (0.5 Tesla), this splitting falls between 40 and 50 K. This freezing temperature is in line with previous measurements, and we have observed this feature across all thickness and batches of films we have investigated. The blue symbols with error bars in Fig. 4(a) were measured via polarized neutron magnetometry in an applied field of 3 T. These agree well with the SQUID data at nearly all measured temperatures. The inset of Fig. 4(a) shows magnetization, M, vs applied field, H(plotted with units of emu/cc, 1 emu/cc = 1 kA/m) for three temperatures, showing linear behavior at 300 K, with slight deviations at lower T on either side of the freezing temperature. As expected for a disordered material with strong antiferromagnetic exchange interactions, nearly any laboratory-scale magnetic field is insufficient to significantly magnetize the material, and no approach to saturation is seen.

Figures 4(b) and 4(c) compare inverse susceptibility,  $\chi^{-1}$  vs T for two a-Y-Fe-O films with 200 nm thickness, grown in two ferent. Sample 1 [Fig. 4(b)] shows two fairly distinct regimes of linear behavior, which one can view as two distinct exchange strengths, as indicated by two different Curie–Weiss  $\theta$ , as seen by  $\frac{9}{8}$ the linear fits shown in blue and green. Both are large and negative, indicating antiferromagnetic exchange. Sample 2 shows a different overall magnitude, with a smaller  $\chi$  (larger  $\chi^{-1}$ ), and is better characterized by the single  $\theta$  with the lower value near 70 K. This suggests that despite the consistent observation of the freezing temperature, there is some degree of variability in the disordered magnetic landscape that can occur from sample-to-sample. Figure 4(d) compares M vs H at 300 K for a-Y-Fe-O (red symbols, on right y axis) to the saturation magnetization value for bulk crystalline YIG (green dashed line, on left y axis). Note that these axes represent very different ranges of M such that the maximum value observed for a-Y-Fe-O is < 1% of the YIG saturation magnetization, again as expected due to the

disorder, strong antiferromagnetic exchange interactions, and resulting high degree of frustration.

Figure 5 presents additional details of polarized neutron reflectometry results on a-Y-Fe-O. Figure 5(a) plots the spindependent reflectivities multiplied by neutron wavevector Q to the 6th power vs Q, measured at  $T = 5 \,\mathrm{K}$  in a 3 T applied field. The use of RQ6 allows better visualization of the data across the entire measured Q range. The data are feature-rich but dominated by nuclear contributions to the scattering. Here, green (purple) symbols present the -- (++) spin analyzed non-spin flip reflectivities. In both, the low Q range shows well-resolved oscillations, due almost entirely to the nuclear contrast. The small sample magnetization results in only a faint spin dependence of the reflectivities. The magnetic signal is better visualized as spin asymmetry,  $(R_{++} - R_{--})/(R_{++} + R_{--})$ , as shown in Fig. 5(b), along with example fitted data measured at higher temperatures. This reveals an unambiguously spin-dependent neutron reflectivity below  $Q \simeq 0.3 \,\mathrm{nm}^{-1}$ . We measured the spin asymmetry in 3 T at four different temperatures, which show a clear T dependence of the

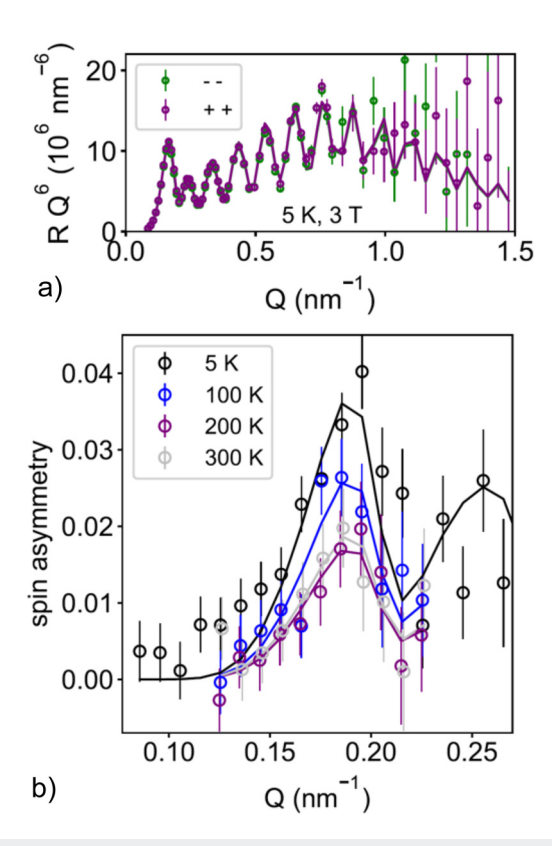


FIG. 5. (a) Non-spin flip neutron reflectivities R multiplied by neutron wavevector  $Q^6$  vs Q for both spin up ++ (purple symbols) and spin down Despite clear oscillations at low Q dominated by nuclear contrast, which are consistent with a scattering density slightly reduced from expectations of bulk YIG, no magnetic contrast is visible without further analysis. (b) 3 T PNR data plotted as spin asymmetry vs Q highlight the temperature-dependent magnetic contribution to the scattering.

peak near  $Q = 0.17 \,\mathrm{nm}^{-1}$ . This demonstrates sensitivity to the temperature dependence of the very weak a-Y-Fe-O magnetization. Fitting this peak allows calculation of the average magnetization of the sample, which is compared to the  $\chi$  measured by SQUID magnetometry above. The PNR data are well-fit by a model with a single 55 nm thick a-Y-Fe-O layer magnetized at 10 emu/cc at 5 K and dropping to 5 emu/cc at 300 K. Thus, while the a-Y-Fe-O film is known to be locally disordered, PNR measurements show that it is a vertically uniform magnetic medium.

Figure 6 compares photoluminescence (PL) vs excitation photon wavelength for a 200 nm thick a-Y-Fe-O film to a bulk polycrystalline YIG substrate. This substrate is the same as commonly employed for thermal probes of spin transport and spincharge conversion via the longitudinal spin Seebeck effect. 45-49 polycrystalline YIG is dominated by a broad and approximately symmetric peak near  $600 \, \text{nm} \cong 2.1 \, \text{eV}$ . This is generally in line with expectations though does suggest a reduction in bandgap from the typical bulk value, as seen in epitaxial YIG thin films. The disordered film shows a much smaller and somewhat broadened PL peak, centered at roughly the same frequency. The reduction in  $\frac{\omega}{\delta}$ intensity is often reported for amorphous semiconductors, though the details of the processes involved can depend sensitively on sample preparation. 50,51 The additional spectral weight above 700 nm could be caused by either localized states below the mobility edge or other mid-gap states, as expected for a disordered semiconductor. It is also possible that a small fraction of polycrystalline domains exist in the amorphous film, which then contribute similar PL spectra, though previous examinations of the a-Y-Fe-O films with typical laboratory x-ray diffraction techniques showed no detectable Bragg peaks.<sup>2</sup>

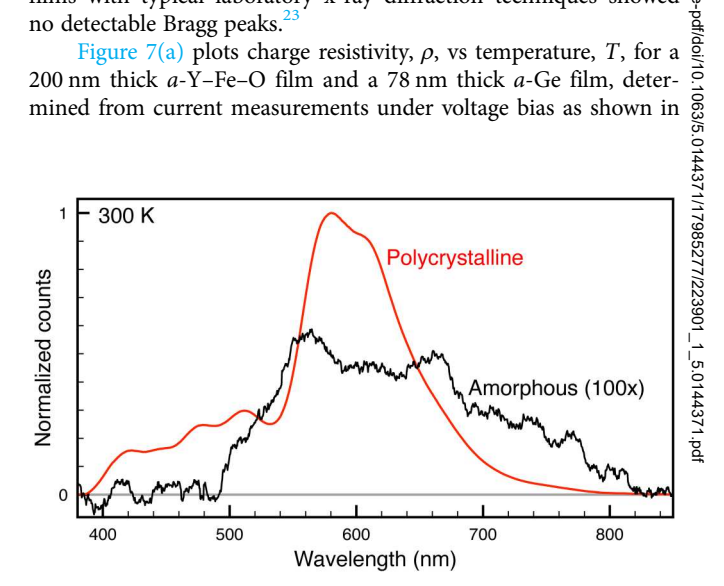
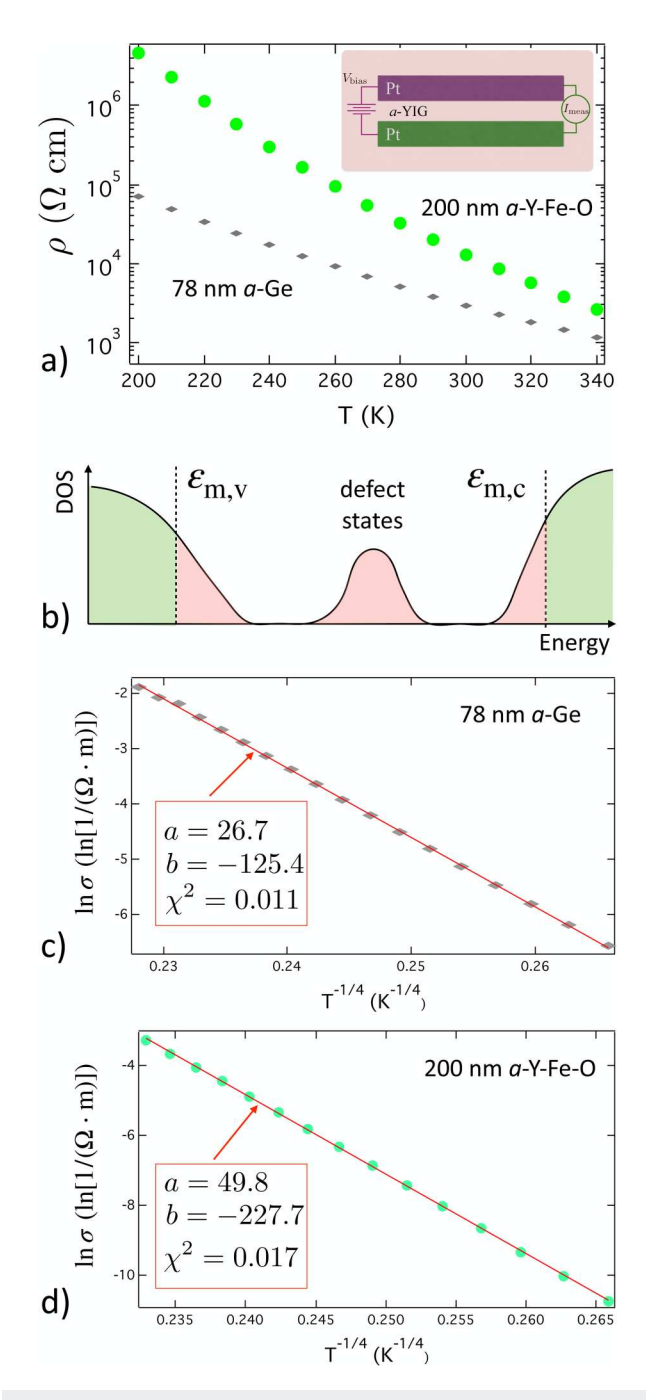


FIG. 6. Comparison of optical photoluminescence vs  $\boldsymbol{\lambda}$  of a bulk polycrystalline substrate (red line) and 200 nm thick a-Y-Fe-O sample (black line, 100×) at 300 K. The somewhat assymetric peak indicates the band edge of the polycrystalline YIG is likely somewhat reduced from tabulated values. The much weaker and broader peak in a-Y-Fe-O indicates optical absorption at similar energies, but with the a broad tail at the low energy (high  $\lambda$ ) side. This is consistent with expectations of a disordered semiconductor.



**FIG. 7.** Charge resistivity  $\rho$  vs T from 200 to 340 K for both 200 nm thick a-Y-Fe-O and 78 nm thick a-Ge. Inset: Schematic view of the voltage-biased measurements used to determine the large values of R which were converted to  $\rho$ . (b) DOS vs energy for an amorphous semiconductor showing extended states in green, the mobility edges  $\varepsilon_{\text{m,v}}$ , and  $\varepsilon_{\text{m,c}}$  and localized states in red, which include a large density of defect states near the center of the gap. (c) and (d)  $\ln \sigma$  vs  $T^{-1/4}$  for a-Ge [panel (c)] and a-Y-Fe-O [panel (d)] show linear behavior  $\ln \sigma = a + b(T^{-1/4})$ , indicating charge transport via variablerange hopping. Linear fit parameters and  $\chi^2$  are indicated for each fit.

the inset schematic. Both materials have large  $\rho$  in this T range spanning room temperature, but are significantly lower than values reported for both bulk YIG and epitaxial thin film YIG, which have  $\rho > 10^7 \,\Omega$  cm at 300 K.<sup>20</sup> As discussed above, this reduced  $\rho$  or increased electrical conductivity,  $\sigma$ , is often a consequence of the formation of defect states in the gap as shown in the schematic density of states vs energy diagram shown in Fig. 7(b). Here, we also indicate the mobility edges,  $\varepsilon_{m,c}$  and  $\varepsilon_{m,v}$ , that divide localized from extended states in the conduction and valence band edges, respectively. Electrical conductivity in a-Ge is dominated by variable-range hopping in these localized states for temperatures near and below room temperature. 32,52,53 Figures 7(c)-7(d) demonstrate charge conduction dominated by variable-range hopping via these localized states in both the a-Ge and a-Y-Fe-O films. These plots show  $\ln \sigma$  vs  $T^{-1/4}$ , with linear least-squares fit lines showing excellent agreement with variable-range hopping [Eq. (1)] over the 200 K > T > 340 K temperature range. Fit parameters and resulting  $\chi^2$  values are indicated in each plot. We also attempted fits to a simple thermal activation model, where  $\ln \sigma$  would be proportional to 1/T. These resulted in poor agreement, with  $\chi^2$  an order of magnitude or more larger than the hopping fits. It is possible to achieve nitude or more larger than the hopping fits. It is possible to achieve better agreement if one assumes two regimes form in T, with different activation energies. Such a view is not out of the question for disordered conductors of various sorts,  $^{54,55}$  and a definitive determination of the transport mechanisms in the a-Y-Fe-O would require a more comprehensive study. Regardless of the exact mechanism, electrical conductivity in the a-Y-Fe-O at levels that can be a solution of the transport mechanisms in the a-Y-Fe-O at levels that can be a solution of the transport mechanism. disordered conductors of various sorts, 54,55 and a definitive deteraffect non-local transport is clear.

affect non-local transport is clear.

Before detailing the consequences of this hopping conductivity on non-local transport experiments, we first clarify the effective ac nature of the "delta mode" and differential conductance measurements performed with the Keithley nanovoltmeter (NVM) and current source. In Fig. 8, we compare a series of electrical measurements on Pt strips formed via EBL on a highly insulating 500 nm Si–N layer deposited on a Si substrate. These strips, with geometry shown schematically in the inset to Fig. 8(a), have the same layout as the device shown in Fig. 3(a), with a "guard rail" Pt strip placed between the injector and detector strips, and the charge resistance between the Pt strips is unmeasurably large at all T described here. In Fig. 8(a), we present the non-local voltage determined by numerical integration of the differential conductance voltage measured with the Keithley NVM in response to a series of excitation 150. sured with the Keithley NVM in response to a series of excitation of currents,  $I_{\text{bias}}$ , sourced by the linked Keithley current source. In this measurement mode and the related "delta mode," the timing between voltage measurements is affected by a parameter  $\frac{1}{2}$ termed "delay time" by the manufacturer. Figure 8(a) plots curves acquired for four different choices of this parameter, ranging from 2 ms (the shortest possible value to 20 ms). Strikingly, the non-local VI curve has the negative slope often associated with spin transport in experiments with a spin conductive media (obviously absent here). The slope of the curve also clearly depends on the choice of the value of the delay time. High values of this parameter (not shown) begin to display an apparent oscillatory response, though the overall negative slope vanishes.

Measurement of the same exact Si-N device in the same cryostat with controlled ac excitation of  $I_{\rm rms} \simeq 75 \,\mu{\rm A}$  and detection of  $V_{\rm nl}$  with a lock-in amplifier indicate that the apparent negative VI

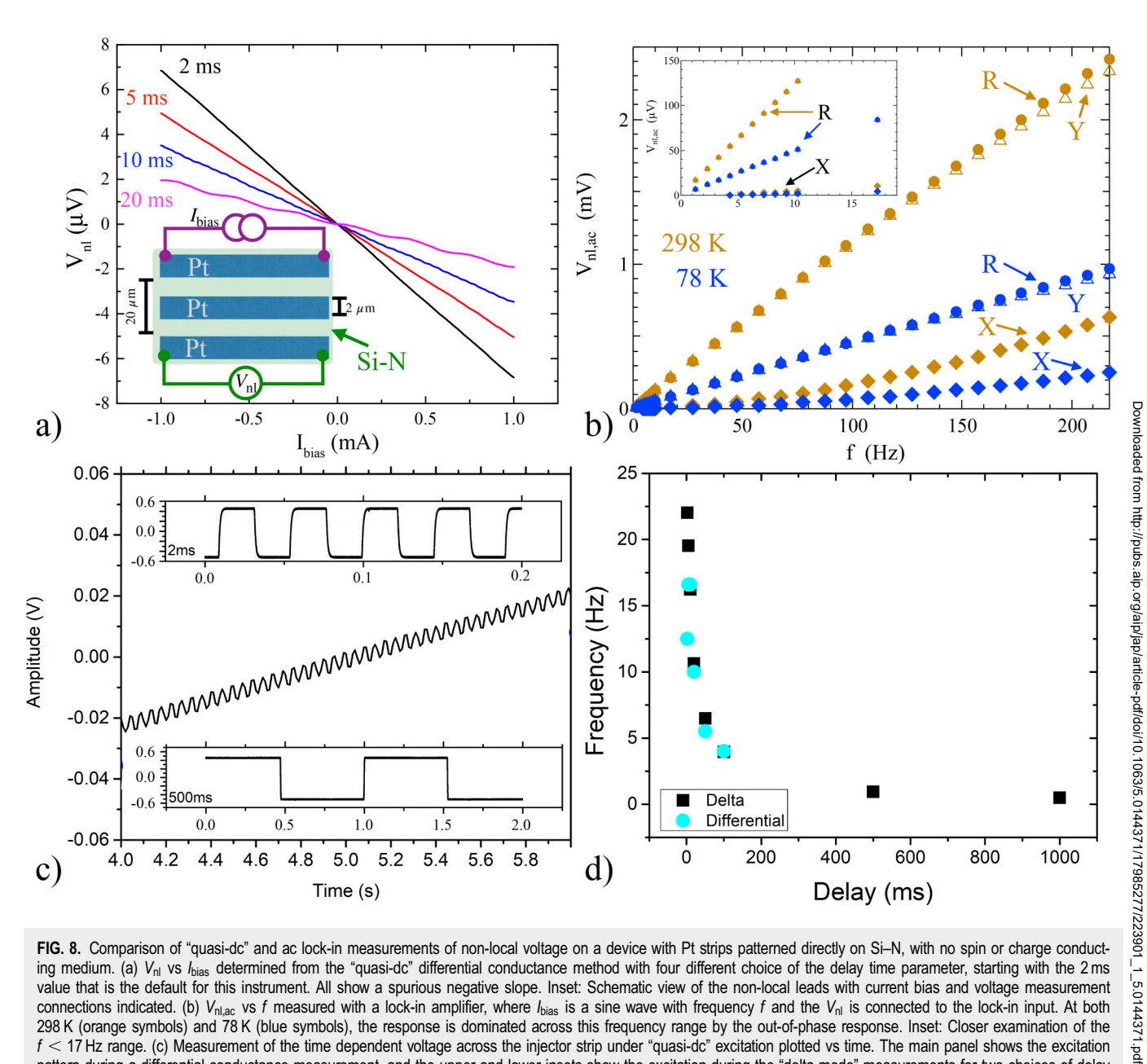


FIG. 8. Comparison of "quasi-dc" and ac lock-in measurements of non-local voltage on a device with Pt strips patterned directly on Si-N, with no spin or charge conducting medium. (a)  $V_{\rm nl}$  vs  $I_{\rm bias}$  determined from the "quasi-dc" differential conductance method with four different choice of the delay time parameter, starting with the 2 ms value that is the default for this instrument. All show a spurious negative slope. Inset: Schematic view of the non-local leads with current bias and voltage measurement connections indicated. (b)  $V_{n,lac}$  vs f measured with a lock-in amplifier, where  $I_{bias}$  is a sine wave with frequency f and the  $V_{nl}$  is connected to the lock-in input. At both 298 K (orange symbols) and 78 K (blue symbols), the response is dominated across this frequency range by the out-of-phase response. Inset: Closer examination of the f < 17 Hz range. (c) Measurement of the time dependent voltage across the injector strip under "quasi-dc" excitation plotted vs time. The main panel shows the excitation pattern during a differential conductance measurement, and the upper and lower insets show the excitation during the "delta mode" measurements for two choices of delay time, as indicated in the insets. (d) Effective frequency of the "quasi-dc" measurements determined from time dependent measurements plotted vs the delay time

slope measured by the "quasi-dc" method is an artifact arising from a large reactive component of the effective circuit. Figure 8(b) shows measured ac voltage response,  $V_{\rm nl,ac}$ , to a well-defined ac bias current, including the in-phase component, X, out-of-phase component, Y, and the total magnitude,  $R = \sqrt{X^2 + Y^2}$  for two different base temperatures, 298 and 78 K. Despite a relatively low f, the out-of-phase component dominates the response at all f and T

shown here. This is seen clearly by R and subsequently Y having much larger values than the in-phase response X. Note that measurements of a resistive load (for example, when both excitation current and voltage detection are attached to a single Pt strip) are dominated by the in-phase component, as expected. This large out-of-phase component of the response is perhaps not surprising when neither charge nor spin can flow from injector to detector,

leaving capacitive and inductive coupling as the only mechanisms for modifying the detected voltage. However, the large reactive component presents a special challenge for the measurement.

Figure 8(c) plots the current excitation from the Keithley current source during the "delta mode" or differential conductance vs time. The main plot shows the current ramp used during a differential conductance measurement, while the top and bottom insets show the current excitation used in "delta mode" for two different choices of the "delay time" parameter discussed above. All of these signals are better understood as low-frequency ac excitations. We explicitly measure the period of these signals for a range of the "delay time" parameter and plot the resulting ac frequency vs the delay time in Fig. 8(d). This shows that the default, short delay time used in these measurements is the functional equivalent of exciting a device with a square wave with f between 5 and 22 Hz. As we show in Fig. 8(b) and is typical in non-local measurements of spin transport through nominally insulating systems, 15 at these frequencies, the Si-N device is dominated by out-of-phase response. This explains the apparent sign inversion of the resistance as determined either from the VI curves measured with the Keithley differential conductance mode or the resistance reported by the "delta mode." Here, the dc NVM is sampling an effective ac

response at a time where the ac voltage has swung out-of-phase. Such a signal can, therefore, not be taken as strong evidence of spin transport without additional verification from magnetic field dependence or other control experiments.

Figure 9 compares non-local voltage measurements made with quasi-dc and ac lock-in techniques when an amorphous germanium film is placed beneath the metal strips. The quasi-dc measurements, measured at a delay time of 2 ms, compare four different strip geometries, shown schematically in the insets in Figs. 9(a) and 9(b). Figure 9(a) compares two "unguarded" geometries with strips separated by distance  $L \cong 20 \,\mu\text{m}$ . The gray line presents results with both Pt injector and detector, where the copper-colored line was measured with Pt injector and a copper detector. Both curves have a positive slope at  $I_{\text{bias}} = 0$ , which could be interpreted as arising from charge leakage through the Ge. The values of these slopes, determined from the linear term of a polynomial fit to the curves, define the first-order non-local resistance  $R_{1,nl}$  and are given for each curve in the figures. The lower voltage and smaller slope for the Cu detector, seen in the values from linear fits that are indicated in the figure, could arise from the lower resistance of the Cu detector strip, as suggested in Eq. (3).

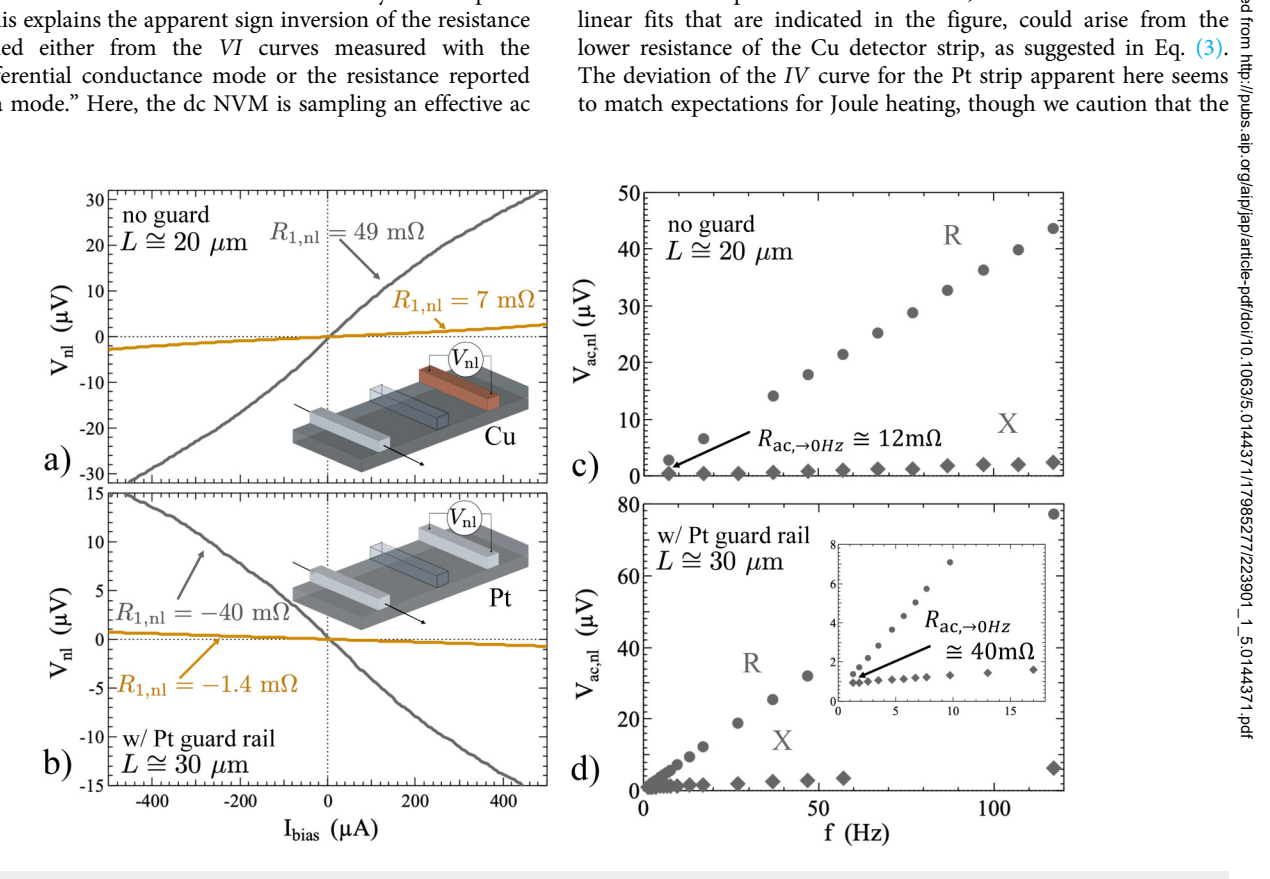


FIG. 9. Non-local voltage measurements on 75 nm thick a-Ge. (a)  $V_{\rm nl}$  vs  $I_{\rm bias}$  using the "quasi-dc" measurement with Pt injector and Pt detector strips with  $L \cong 20\,\mu{\rm m}$ (grey line) and using a Pt injector and Cu detector (orange line). Inset: Schematic view of the non-local setup with a Cu detector, with the possible third "guard rail" strip shown in outline. (b) Similar  $V_{nl}$  vs  $I_{bias}$  measured with "quasi-dc" approach with the additional third strip in place. An apparent inversion of the sign of the non-local resistance occurs. (c) Lock-in amplifier measurements of the same device with Pt strips and no "guard rail,"  $V_{ac,nl}$  vs f with ac excitation  $I_{ms} \cong 5\mu A$  (similar behavior occurs for larger excitations). As seen on Si-N, the signal is dominated by an out-of-phase component. (d) Lock-in measurements of the device with the third Pt strip added, where the out-of-phase component is significantly increased. No negative values of non-local resistance are observed. Inset: Closer view of the t < 17 Hz range shows the in-phase component always remains below the total signal magnitude.

Downloaded from http://pubs.aip.org/aip/jap/article-pdf/doi/10.1063/5.0144371/17985277/223801\_1

presence of the electrical artifacts related to the quasi-dc measurement complicate such an interpretation. Figure 9(b) shows similar data but with the additional Pt strip placed between the injector and detector, while somewhat increasing the overall distance between injector and detector at  $L \cong 30\,\mu\mathrm{m}$ . Here, both quasi-dc VI curves invert sign, though the Cu detector again shows much smaller values than the Pt. Without confirmation from the ac lock-in measurements, this pattern could be interpreted as evidence of spin transport, clarifying the importance of the more controlled frequency-dependent non-local voltage measurements shown at right.

Figures 9(c) and 9(d) present  $V_{ac,nl}$  vs f measured with a lock-in amplifier again on the same device with the same Pt strips and the same cryostat wiring. As with the control experiment on Si-N, the ac voltage is dominated by a large out-of-phase component, with X < R even at frequencies below 10 Hz. This is true for both the case with no third Pt strip [panel (c)] and when the "guard rail" is inserted [panel (d)]. Note the larger  $V_{\rm ac,nl}$  range in (d), indicating as in the Si-N case that one major consequence of the additional Pt strip is to increase the reactive components of the overall circuit, leading to a larger out-of-phase component. The inset shows a closer view of the low f region, again clarifying that the in-phase portion of the response is always less than the reactive, out-of-phase component. With the third Pt strip in place, at the ≈ 17 Hz effective frequency of the quasi-dc IV measurement, the out-of-phase component is 10× greater than the in-phase response. Without the third Pt strip, the out-of-phase response still dominates, but R is roughly half of the three-strip value. This significant shift in the reactive impedance drives the false inversion of sign between the experimental conditions of Figs. 9(a) and 9(b).

In Figs. 9(c) and 9(d), we also indicate the value of the nonlocal resistance determined from the in-phase ac voltage component for the two-strip "no guard" and three-strip "w/Pt guard rail" cases, extrapolated to zero f based only on the lowest frequency data points. If the Pt strip between injector and detector was actually acting to shield the detector from charge leakage, one would expect this value to be dramatically lower in the "guard rail" case. The experimental values provide no evidence of this, as  $R_{ac,\rightarrow 0\,\mathrm{Hz}}$ instead increases by a factor of  $2-4\times$  when the third Pt strip is added, and the overall distance between injector and detector increases. Though we caution that determining the true dc resistance accurately is difficult when such large reactive components of the circuit are present, the pattern shown here provides no clear evidence of the "guard rail" effect. The increase in  $R_{ac,\to 0\,\mathrm{Hz}}$  upon adding a strip and increasing L does not have a simple interpretation as charge leakage in a uniform conducting medium.

We now use the same two measurement techniques to examine non-local voltage measurements on a-Y-Fe-O films. Figure 10 presents VI curves measured on "no guard" [panel (a)] and "w/Pt guard rail" geometries [panel (b)], taken with the quasi-dc technique with delay time of 2 ms (an effective ac excitation with  $f \cong 17 \, \text{Hz}$ ). As with our original work, <sup>23</sup> these a-Y-Fe-O films were deposited on top of a pattern of wider and longer Pt strips, as shown in Figs. 3(c) and 3(d). <sup>56</sup> As in the case of the a-Ge, the two Pt strip "no guard" geometry shows a positive slope, but the additional strip inverts the sign of the apparent non-local resistance. Similar patterns with different overall magnitudes (not

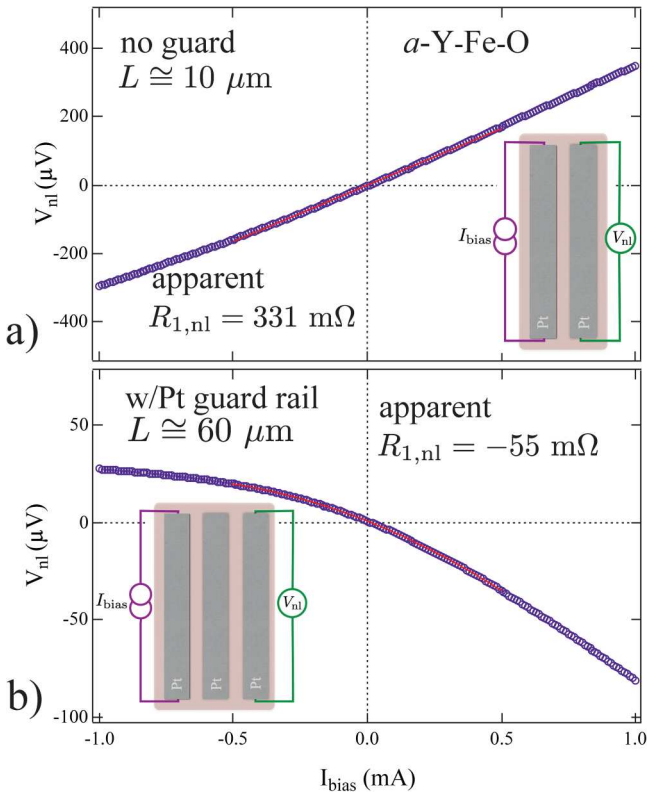


**FIG. 10.** Non-local voltage  $V_{\rm nl}$  vs  $I_{\rm bias}$  measured using the "quasi-dc" approach on a-Y-Fe-O using (a) only two Pt strips and (b) with the addition of a third Pt "guard rail." As seen in the a-Ge case, an apparent inversion of the non-local resistance occurs. Red lines in both panels show the polynomial fit used to extract the linear component,  $R_{\rm 1,nl}$ . For both cases, the fit was performed from -0.5 to 0.5 mA. Insets: Schematic views of the lead geometries used in each panel.

shown) occur in a device with 100 nm thick a-Y-Fe-O. However, as with the a-Ge, the sign inversion cannot be interpreted as evidence of spin transport before closer examination of the frequency dependence.

dependence.

Figures 11(a) and 11(b) compare the total ac lock-in voltage response, R [panel (a)] and in-phase component X [panel (b)] vs f for three-strip geometries patterned via EBL on top of a 200 nm thick a-Y-Fe-O with the layout shown in Fig. 3(a). As seen in both Si-N and a-Ge, large out-of-phase components of the signal dominate a much smaller in-phase response, with X approaching zero as f drops. For a-Y-Fe-O, the in-phase response also has a clear component  $\infty f^2$ . This is also true for the corresponding Si-N and a-Ge, though less obvious in Figs. 8 and 9. This  $f^2$  dependence could be explained by a second leakage path into the detector strip, through a parallel capacitance. Simple attempts to model this effect suggest fairly large capacitances, well in excess of the value we calculate based on the geometry of the conducting strips alone. This could indicate that interfacial capacitances from Schottky barrier effects between the metal strips and the samples play an important

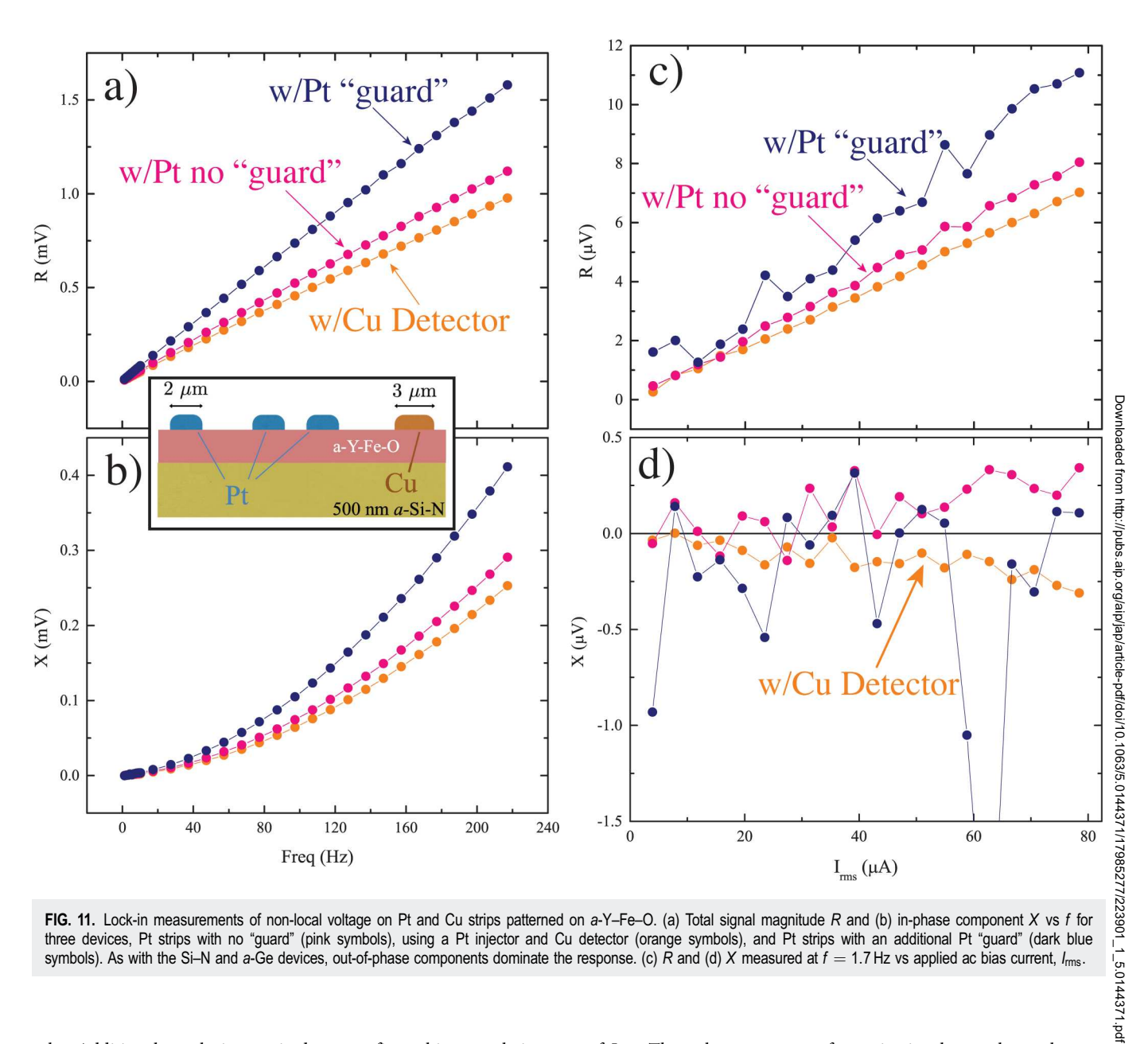


FIG. 11. Lock-in measurements of non-local voltage on Pt and Cu strips patterned on a-Y-Fe-O. (a) Total signal magnitude R and (b) in-phase component X vs f for three devices, Pt strips with no "guard" (pink symbols), using a Pt injector and Cu detector (orange symbols), and Pt strips with an additional Pt "guard" (dark blue symbols). As with the Si-N and a-Ge devices, out-of-phase components dominate the response. (c)  $\tilde{R}$  and (d) X measured at  $f=1.7\,\mathrm{Hz}$  vs applied ac bias current,  $I_{\mathrm{rms}}$ .

role. Additional work is required to confirm this speculation. Importantly, the pattern of R in panel (a) shows that adding the third Pt strip increases the reactive impedance, as seen with a-Ge, which again will introduce artificial sign change in the effective 17 Hz measurement of Fig. 10. The lower resistance of the Cu detector drops both the in-phase and out-of-phase component of the signal, though the dominant component remains the out-of-phase reactive load.

In Figs. 11(c) and 11(d), we plot R and X at f = 1.7 Hz vs ac bias current  $I_{rms}$  for the same three-strip geometries. While the reactive components increase roughly linearly with increasing current, the in-phase component stays essentially zero as a function of  $I_{\rm rms}$ . The only appearance of negative in-phase voltage, the true condition for observation of non-local resistance consistent with spin transport, comes at higher  $I_{rms}$  but for the Cu detector strip, where the small spin Hall angle suggests spin transport should not generate a voltage. Note also that the additional Pt "guard rail" could be seen as somewhat reducing the in-phase signal from charge leakage, though the main effect is to increase the noise and there is still not strong evidence of the effectiveness of this approach, at least for the lead geometries we implemented here.

Figure 12 presents ac lock-in measurements on the simplest two-strip geometry with the smallest L we examined, at  $2\mu m$ , measured for five T, at a larger bias current  $I_{\rm rms} \sim 7$  mA. Figures 12(a)

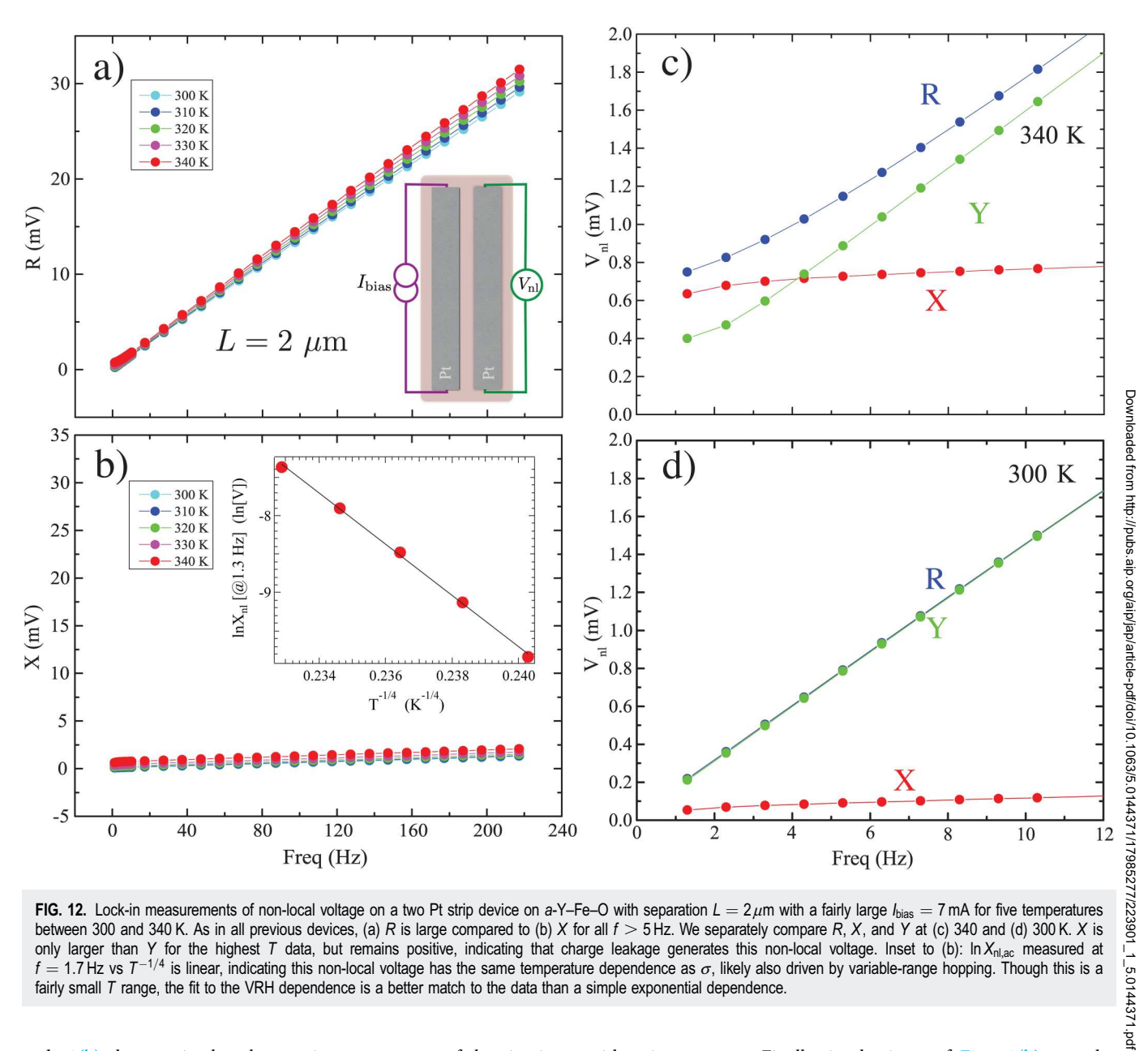


FIG. 12. Lock-in measurements of non-local voltage on a two Pt strip device on a-Y-Fe-O with separation  $L=2\,\mu\mathrm{m}$  with a fairly large  $I_{\mathrm{bias}}=7\,\mathrm{mA}$  for five temperatures between 300 and 340 K. As in all previous devices, (a) R is large compared to (b) X for all f > 5 Hz. We separately compare R, X, and Y at (c) 340 and (d) 300 K. X is only larger than Y for the highest T data, but remains positive, indicating that charge leakage generates this non-local voltage. Inset to (b): ln X<sub>nl,ac</sub> measured at f=1.7 Hz vs  $T^{-1/4}$  is linear, indicating this non-local voltage has the same temperature dependence as  $\sigma$ , likely also driven by variable-range hopping. Though this is a fairly small T range, the fit to the VRH dependence is a better match to the data than a simple exponential dependence.

and 12(b) show again that the reactive components of the circuit dominate the in-phase resistive components at all but the very lowest f, and certainly at the  $\cong$  17 Hz effective excitation frequency of the default Keithley delta mode and differential conductance measurements. Figures 12(c) and 12(d) plot X, Y, and R at low f for two temperatures, 340 [panel (c)] and 300 K [panel (d)]. We see that only at elevated T, where the charge conductivity of the a-Y-Fe-O has increased significantly, and for  $f < 5 \,\mathrm{Hz}$  does the in-phase response exceed the out-of-phase response in the lock-in measurement. This is similar to the case for measurements of nonlocal spin transport in epitaxial YIG15 though in a-Y-Fe-O, the positive sign here indicates charge leakage and is not consistent with spin transport. Finally, in the inset of Fig. 12(b), we plot  $\ln{(X)}$  measured at  $f=1.7\,\mathrm{Hz}$  vs  $T^{-1/4}$ . Across this somewhat limited range of T, these points are well-explained by a straight line, indicating that the temperature dependence of the resistive response of the device is the same as for variable-range hopping, Eq. (1), providing additional confirmation that charge leakage is the physical origin of the only reliable resistive response measured in these non-local experiments.

Contrary to our original work<sup>23</sup> and in line with later investigations of non-local voltage measurements in a-Y-Fe-O by other groups, 24,25 this more complete and detailed investigation shows no evidence consistent with spin transport in this speromagnetic

disordered semiconductor over micrometer length scales. Furthermore, the charge transport we have clearly identified should be considered in experiments that claimed spin transport across much thinner a-Y-Fe-O layers.<sup>21</sup>

#### V. CONCLUSION

In summary, we presented charge resistivity and conductivity measurements on a-Y-Fe-O and a-Ge films in geometries used for non-local voltage measurements. These show that both these materials should be viewed as amorphous semiconductors with charge conductivity dominated by variable-range hopping. We also presented optical photoluminescence measurements that supported this conclusion. We also presented simple analytic models to help explain how charge leakage through such a medium can lead to signals in non-local voltage measurements that originate purely from charge. We presented magnetic characterization that shed light on the disordered magnetism in a-Y-Fe-O. We also compared two experimental techniques to carry out non-local voltage measurements, including control measurements on Pt strips patterned on a Si-N coated Si substrate and Pt and Cu strips patterned on the a-Ge thin film. These show clearly that the fairly common automated "quasi-dc" measurement carried out with a linked nominally dc current source and nanovoltmeter actually applies an ac current with frequency 22 Hz in the common default settings, and that this frequency falls in a range where our non-local voltage devices are dominated by reactive contributions to the circuit. This has the consequence that an inversion of the sign of a measured IV curve can occur. This suggests strongly that when measurements with these "quasi-dc" techniques are used, the sign inversion itself is not sufficient to prove spin transport in a given device. Finally, we carried out both "quasi-dc" and truly ac lock-in detected measurements of non-local voltages in a-Y-Fe-O. Contrary to our group's original claim and in line with more recent measurements from others, we see no evidence for spin transport across micrometer-scale distances in this disordered magnetic semiconductor.

### **ACKNOWLEDGMENTS**

We acknowledge M. Natale, R. K. Bennet, and D. J. Wesenberg for helpful discussions, assistance in the lab, and contributions to early experiments, and Tao Liu for sample preparation. We gratefully acknowledge support from the NSF (Nos. DMR-1709646 and DMR-2004646). Work at CSU was supported by the U.S. National Science Foundation (Nos. ECCS-1915849 and DMR-2002980). Contributions by G.D. to this research were supported by an appointment to the Intelligence Community Postdoctoral Research Fellowship Program at University of Washington and administered by Oak Ridge Institute for Science and Education through an interagency agreement between the U.S. Department of Energy and the Office of the Director of National Intelligence.

# **AUTHOR DECLARATIONS**

### Conflict of Interest

The authors have no conflicts to disclose.

### **Author Contributions**

M.J.R., S.M.B., and L.H. have contributed equally to this paper.

M. J. Roos: Conceptualization (equal); Data curation (equal); Formal analysis (equal); Investigation (equal); Methodology (equal); Software (equal). S. M. Bleser: Conceptualization (equal); Data curation (equal); Formal analysis (equal); Investigation (equal); Methodology (equal); Software (equal); Visualization (equal). L. Hernandez: Conceptualization (equal); Data curation (equal); Formal analysis (equal); Investigation (equal); Methodology (equal); Software (equal). G. M. Diederich: Conceptualization (supporting); Formal analysis (supporting); Investigation (supporting); Methodology (supporting). M. E. Siemens: Conceptualization (supporting); Methodology (supporting); Supervision (supporting); Visualization (supporting); Writing ing); Supervision (supporting); v isualization (supporting); review & editing (supporting). M. Wu: Investigation (supporting); Writing – review Resources (supporting); Supervision (supporting); Writing - review & editing (supporting). **B. J. Kirby:** Conceptualization (supporting); Data curation (supporting); Formal analysis (supporting); Investigation (supporting); Methodology (supporting); Visualization (supporting); Writing - review & editing (supporting). B. L. Zink: Funding acquisition (lead); Methodology (lead); Project administration (lead); Supervision (lead); Validation (lead); Writing – original

- tion (lead); Supervision (lead); Validation (lead); Writing original draft (lead); Writing review & editing (lead).

  DATA AVAILABILITY

  The data that support the findings of this study are available from the corresponding author upon reasonable request.

  REFERENCES

  1 M. Althammer, "All-electrical magnon transport experiments in magnetically ordered insulators," Phys. Status Solidi 15, 2100130 (2021).
  2 H. Wang, C. Du, P. C. Hammel, and F. Yang, "Antiferromagnonic spin transport from Y<sub>3</sub>Fe<sub>5</sub>O<sub>12</sub> into NiO," Phys. Rev. Lett. 113, 097202 (2014).
  3 C. Hahn, G. de Loubens, V. V. Naletov, J. B. Youssef, O. Klein, and M. Viret, "Conduction of spin currents through insulating antiferromagnetic oxides," Europhys. Lett. 108, 57005 (2014).
  4 B. L. Zink, M. Manno, L. O'Brien, J. Lotze, M. Weiler, D. Bassett, S. J. Mason, S. T. B. Goennenwein, M. Johnson, and C. Leighton, "Efficient spin transport through native oxides of nickel and permalloy with platinum and gold overlayers," Phys. Rev. B 93, 184401 (2016). layers," Phys. Rev. B 93, 184401 (2016).
- <sup>5</sup>W. Lin, K. Chen, S. Zhang, and C. L. Chien, "Enhancement of thermally 2 injected spin current through an antiferromagnetic insulator," Phys. Rev. Lett. 116, 186601 (2016).
- 6G. R. Hoogeboom, G.-J. N. S. Nicolaas, A. Alexander, O. Kuschel, € J. Wollschläger, I. Ennen, B. J. van Wees, and T. Kuschel, "Role of NiO in the nonlocal spin transport through thin NiO films on Y<sub>3</sub>Fe<sub>5</sub>O<sub>12</sub>," Phys. Rev. B 103,
- <sup>7</sup>J. Han, P. Zhang, Z. Bi, Y. Fan, T. S. Safi, J. Xiang, J. Finley, L. Fu, R. Cheng, and L. Liu, "Birefringence-like spin transport via linearly polarized antiferromagnetic magnons," Nat. Nanotechnol. 15, 563-568 (2020).
- <sup>8</sup>W. Yuan, Q. Zhu, T. Su, Y. Yao, W. Xing, Y. Chen, Y. Ma, X. Lin, J. Shi, R. Shindou, X. C. Xie, and W. Han, "Experimental signatures of spin superfluid ground state in canted antiferromagnet Cr2O3 via nonlocal spin transport," Sci. Adv. 4, eaat1098 (2018).
- <sup>9</sup>R. Lebrun, A. Ross, S. A. Bender, A. Qaiumzadeh, L. Baldrati, J. Cramer, A. Brataas, R. A. Duine, and M. Kläui, "Tunable long-distance spin transport in a crystalline antiferromagnetic iron oxide," Nature 561, 222-225 (2018).

"Spin-current-controlled modulation of the magnon spin conductance in a three-terminal magnon transistor," Phys. Rev. Lett. 120, 097702 (2018).

12H. Wu, L. Huang, C. Fang, B. S. Yang, C. H. Wan, G. Q. Yu, J. F. Feng, H. X. Wei, and X. F. Han, "Magnon valve effect between two magnetic insulators," Phys. Rev. Lett. 120, 097205 (2018).

13 J. Shan, A. V. Singh, L. Liang, L. J. Cornelissen, Z. Galazka, A. Gupta, B. J. van Wees, and T. Kuschel, "Enhanced magnon spin transport in NiFe2O4 thin films on a lattice-matched substrate," Appl. Phys. Lett. 113, 162403 (2018).

14J. Shan, L. J. Cornelissen, N. Vlietstra, J. Ben Youssef, T. Kuschel, R. A. Duine, and B. J. van Wees, "Influence of yttrium iron garnet thickness and heater opacity on the nonlocal transport of electrically and thermally excited magnons," Phys. Rev. B 94, 174437 (2016).

15 L. J. Cornelissen, J. Liu, R. A. Duine, J. B. Youssef, and B. J. van Wees, "Long-distance transport of magnon spin information in a magnetic insulator at room temperature," Nat. Phys. 11, 1022-1026 (2015).

16 B. L. Giles, Z. Yang, J. S. Jamison, and R. C. Myers, "Long-range pure magnon spin diffusion observed in a nonlocal spin-Seebeck geometry," Phys. Rev. B 92, 224415 (2015).

17S. T. B. Goennenwein, R. Schlitz, M. Pernpeintner, K. Ganzhorn, M. Althammer, R. Gross, and H. Huebl, "Non-local magnetoresistance in YIG/ Pt nanostructures," Appl. Phys. Lett. 107, 172405 (2015).

18 N. Thiery, A. Draveny, V. V. Naletov, L. Vila, J. P. Attané, C. Beigné, G. de Loubens, M. Viret, N. Beaulieu, J. Ben Youssef, V. E. Demidov, S. O. Demokritov, A. N. Slavin, V. S. Tiberkevich, A. Anane, P. Bortolotti, V. Cros, and O. Klein, "Nonlinear spin conductance of yttrium iron garnet thin films driven by large spin-orbit torque," Phys. Rev. B 97, 060409 (2018).

19Y. Kajiwara, K. Harii, S. Takahashi, J. Ohe, K. Uchida, M. Mizuguchi, H. Umezawa, H. Kawai, K. Ando, K. Takanashi, S. Maekawa, and E. Saitoh, "Transmission of electrical signals by spin-wave interconversion in a magnetic insulator," Nature 464, 262-266 (2010).

<sup>20</sup>N. Thiery, V. V. Naletov, L. Vila, A. Marty, A. Brenac, J.-F. Jacquot, G. de Loubens, M. Viret, A. Anane, V. Cros, J. Ben Youssef, N. Beaulieu, V. E. Demidov, B. Divinskiy, S. O. Demokritov, and O. Klein, "Electrical properties of epitaxial yttrium iron garnet ultrathin films at high temperatures," Phys. Rev. B 97, 064422 (2018).

<sup>21</sup>H. Wang, C. Du, P. C. Hammel, and F. Yang, "Spin transport in antiferromagnetic insulators mediated by magnetic correlations," Phys. Rev. B 91, 220410 (2015). <sup>22</sup>C. L. Chien, see https://meetings.aps.org/Meeting/MAR18/Session/F25.1 for "Thermal magnonic spin current in antiferromagnetic insulator/YIG," APS March Meeting (2018).

<sup>23</sup>D. Wesenberg, T. Liu, D. Balzar, M. Wu, and B. L. Zink, "Long-distance spin transport in a disordered magnetic insulator," Nat. Phys. 13, 987-993 (2017).

<sup>24</sup>J. M. Gomez-Perez, K. Oyanagi, R. Yahiro, R. Ramos, L. E. Hueso, E. Saitoh, and F. Casanova, "Absence of evidence of spin transport through amorphous Y<sub>3</sub>Fe<sub>5</sub>O<sub>12</sub>," Appl. Phys. Lett. **116**, 032401 (2020).

<sup>25</sup>L. Yang, Y. Gu, L. Chen, K. Zhou, Q. Fu, W. Wang, L. Li, C. Yan, H. Li, L. Liang, Z. Li, Y. Pu, Y. Du, and R. Liu, "Absence of spin transport in amorphous YIG evidenced by nonlocal spin transport experiments," Phys. Rev. B 104,

26Y. Tserkovnyak and H. Ochoa, "Generalized boundary conditions for spin transfer," Phys. Rev. B 96, 100402 (2017).

<sup>27</sup>H. Ochoa, R. Zarzuela, and Y. Tserkovnyak, "Spin hydrodynamics in amorphous magnets," Phys. Rev. B **98**, 054424 (2018). <sup>28</sup>E. Iacocca and M. A. Hoefer, "Hydrodynamic description of long-distance

spin transport through noncollinear magnetization states: Role of dispersion,

nonlinearity, and damping," Phys. Rev. B 99, 184402 (2019).

<sup>29</sup>M. Kameda, G. E. W. Bauer, and J. Barker, "Magnon spectrum of the amorphous ferromagnet Co<sub>4</sub>P from atomistic spin dynamics," arXiv:2201.06986 [cond-mat.mes-hall] (2022).

30 J. E. Medvedeva, D. B. Buchholz, and R. P. H. Chang, "Recent advances in understanding the structure and properties of amorphous oxide semiconductors," Adv. Electron. Mater. 3, 1700082 (2017).

31 P. A. Lee and T. V. Ramakrishnan, "Disordered electronic systems," Rev. Mod. Phys. 57, 287-337 (1985).

32N. F. Mott and E. A. Davis, Electronic Processes in Non-Crystalline Materials (OUP, Oxford, 2012).

33J. Gückelhorn, T. Wimmer, S. Geprägs, H. Huebl, R. Gross, and M. Althammer, "Quantitative comparison of magnon transport experiments in three-terminal YIG/Pt nanostructures acquired via dc and ac detection techniques," Appl. Phys. Lett. 117, 182401 (2020).

34R. Sultan, A. D. Avery, G. Stiehl, and B. L. Zink, "Thermal conductivity of micromachined low-stress silicon-nitride beams from 77-325 K," J. Appl. Phys. 105, 043501 (2009).

35R. Sultan, A. D. Avery, J. M. Underwood, S. J. Mason, D. Bassett, and B. L. Zink, "Heat transport by long mean free path vibrations in amorphous silicon nitride near room temperature," Phys. Rev. B 87, 214305 (2013).

36 A. D. Avery, S. J. Mason, D. Bassett, D. Wesenberg, and B. L. Zink, "Thermal and electrical conductivity of approximately 100-nm permalloy, Ni, Co, Al, and Cu films and examination of the Wiedemann-Franz law," Phys. Rev. B 92, 376, 114410 (2015).

37http://www.qdusa.com

38B. Maranville, W. Ratcliff II, and P. Kienzle, "Reductus: A stateless python data reduction service with a browser front end," J. Appl. Crystallogr. 51, 1500-1506 (2018).

39B. Kirby, P. Kienzle, B. Maranville, N. Berk, J. Krycka, F. Heinrich, and C. Majkrzak, "Phase-sensitive specular neutron reflectometry for imaging the  $\frac{\hat{\mathbf{u}}}{\mathbf{p}}$ nanometer scale composition depth profile of thin-film materials," Curr. Opin. Colloid Interface Sci. 17, 44-53 (2012).

40 J. M. D. Coey, Magnetism and Magnetic Materials (Cambridge University Press, Cambridge, 2009).

<sup>41</sup>J. M. D. Coey, "Noncollinear spin structures," Can. J. Phys. **65**, 1210–1232 (1987).

42 J. M. D. Coey and D. Ryan, "Current trends in amorphous magnetism," IEEE Trans. Magn. 20, 1278–1283 (1984).

<sup>43</sup>E. M. Gyorgy, K. Nassau, K. Nassau, M. Eibschutz, J. V. Waszczak, C. A. Wang, and J. C. Shelton, "The magnetic properties of amorphous Y<sub>3</sub>Fe<sub>5</sub>O<sub>12</sub>," J. Appl. Phys. **50**, 2883 (1979).

44Y. G. Chukalkin, V. R. Shtirz, and B. N. Goshchitskii, "The structure and magnetism of amorphous Y<sub>3</sub>Fe<sub>5</sub>O<sub>12</sub>," Phys. Status Solidi A 112, 161-174 (1989).

45K. Uchida, M. Ishida, T. Kikkawa, A. Kirihara, T. Murakami, and E. Saitoh, "Longitudinal spin Seebeck effect: From fundamentals to applications," J. Phys.: Condens, Matter 26, 343202 (2014).

<sup>46</sup>D. Qu, S. Y. Huang, J. Hu, R. Wu, and C. L. Chien, "Intrinsic spin Seebeck effect in Au/YIG," Phys. Rev. Lett. 110, 067206 (2013).

47D. Qu, S. Y. Huang, B. F. Miao, S. X. Huang, and C. L. Chien, "Self-consistent determination of spin Hall angles in selected 5d metals by thermal spin injection," Phys. Rev. B 89, 140407 (2014).

48 T. Wang, W. Wang, Y. Xie, M. A. Warsi, J. Wu, Y. Chen, V. O. Lorenz, X. Fan, and J. Q. Xiao, "Large spin Hall angle in vanadium film," Sci. Rep. 7, 1306

49 S. M. Bleser, R. M. Greening, M. J. Roos, L. A. Hernandez, X. Fan, and B. L. Zink, "Negative spin Hall angle and large spin-charge conversion in thermally evaporated chromium thin films," J. Appl. Phys. 131, 113904 (2022).

<sup>50</sup>R. Street, "Luminescence in amorphous semiconductors," Adv. Phys. 25, 397-453 (1976).

51 R. A. Street, J. C. Knights, and D. K. Biegelsen, "Luminescence studies of plasma-deposited hydrogenated silicon," Phys. Rev. B 18, 1880-1891 (1978).

<sup>152</sup>M. L. Knotek, M. Pollak, T. M. Donovan, and H. Kurtzman, "Thickness dependence of hopping transport in amorphous-ge films," Phys. Rev. Lett. 30, 853-856 (1973).

53 A. Clark, M. M. Cohen, M. Campi, and H. Lanyon, "Magnetoresistance in amorphous germanium," J. Non-Cryst. Solids 16, 117-127 (1974).

<sup>55</sup>D. J. Wesenberg, M. J. Roos, A. D. Avery, J. L. Blackburn, A. J. Ferguson, and B. L. Zink, "Size- and temperature-dependent suppression of phonon thermal

conductivity in carbon nanotube thermoelectric films," Adv. Electron. Mater. 6, 2000746 (2020).

56We note that our original work on *a*-Y-Fe-O non-local resistance used a truly dc current source, stepped with computer control over long enough times to avoid any spurious sign flips. In that work, all the non-local voltages were positive in the sense we define here.